Flow (2025), **5** E2
doi:10.1017/flo.2024.36

FLOW CAMBRIDGE UNIVERSITY PRESS

RESEARCH ARTICLE

A large-eddy simulation study of water tunnel interference effects for a marine propeller in crashback mode of operation

Thomas Bahati Kroll[1] and Krishnan Mahesh[2,*]

[1]Aerospace Engineering & Mechanics, University of Minnesota, Minneapolis, MN 55455, USA
[2]Department of Naval Architecture and Marine Engineering, University of Michigan, Ann Arbor, MI 48109, USA
*Corresponding author. E-mail: krmahesh@umich.edu

Received: 23 October 2024; **Accepted:** 3 December 2024

Keywords: Large-eddy simulation; Overset; Water tunnels; Marine propellers; Crashback; Off-design propeller; Water tunnel interference

Abstract

Marine propellers are studied in design and off-design modes of operation like crashback, where the propeller rotates in reverse while the vehicle is in forward motion. Past experiments (Jessup *et al.*, *Proceedings of the 25th Symposium on Naval Hydrodynamics, St John's, Canada*, 2004; *Proceedings of the 26th Symposium on Naval Hydrodynamics, Rome, Italy*, 2006) studied the marine propeller David Taylor Model Basin 4381 in the open-jet test section of the 36-inch variable pressure water tunnel (VPWT). In crashback, a significant discrepancy with unclear sources exists between the mean propeller loads from the VPWT and open-water towing tank (OW) experiments (Ebert *et al.*, *2007 ONR Propulsor S & T Program Review, October*, 2007). We perform large-eddy simulation at $Re = 561\,000$ and advance ratios $J = -0.50$ and -0.82 with the VPWT geometry included, contrasting to the unconfined (OW) case at those same J and $Re = 480\,000$. We identify and delineate the water tunnel interference effects responsible, and demonstrate that these effects resemble those of a symmetric solid model or bluff body. Solid blockage due to jet expansion and nozzle blockage due to proximity to the tunnel nozzle are identified as the primary interference effects. Their impact varies with the advance ratio J and strengthens for higher magnitudes of J. The effective length scale to assess the severity of interference effects is found to be larger than the vortex ring diameter.

Impact Statement

There is a lack of crashback experimental work in the literature. Computational fluid dynamics through large-eddy simulation and high-performance computing tools have played a crucial role in helping fill the knowledge gap and better unveil its flow physical nature. However, it is essential to match experimental boundary conditions for better validation and to inform better future experimental designs. The present simulations do this by including the water tunnel geometry, and the validated results reveal the flow physics of the underlying tunnel interference effects. The high fidelity of the results and the generality of the unstructured overset grid large-eddy simulation methodology suggest its profitable use to predict a wide range of complex engineering flows.

1. Introduction

Crashback is an off-design operating condition where propeller rotation is reversed as a vehicle is still moving forward to create negative thrust and slow down the vehicle. A prominent flow feature is the

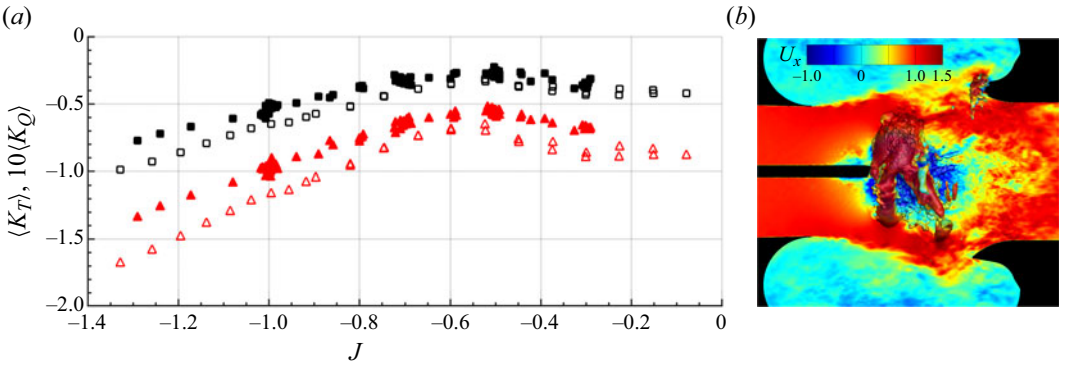

Figure 1. *(a) A plot of the mean of K_T and $10K_Q$ versus J in crashback for an open propeller. Experimental loads from the 36-inch VPWT (Jessup et al. 2004, 2006) and OW (Ebert et al. 2007), where ■ is K_T in VPWT, □ is K_T in OW, ▲ is $10K_Q$ in VPWT and △ is $10K_Q$ in OW. Note the discrepancy between the VPWT and OW which grows as the magnitude of J increases. (b) Crashback ($J = -0.82$): constant z-plane ($z = 0$) slice with contours of instantaneous axial velocity U_x and an iso-contour of pressure coloured by U_x. Note the irregularly shaped vortex ring interacting with the jet shear layer of the 36-inch VPWT nozzle. The flow-field quantities are normalized appropriately using ρ and U_∞.*

unstable vortex ring formed by the interaction of the propeller-induced reverse flow and the forward-moving free stream (figure 1). Locally, the propeller blades experience large flow separation (due to leading- and trailing-edge reversal), resulting in highly unsteady loads with low frequencies and high amplitudes. This has implications on the blade structure as well as on the manoeuvrability of a vessel (Jang & Mahesh 2013).

One way to study propellers in crashback is through scaled-down model experiments. These experiments are performed inside a water tunnel to provide a controlled environment to investigate different propeller conditions and provide verification and performance data which can also be used for the validation of computational codes. Some of the important parameters that are varied are the advance ratio J and Reynolds number Re as defined below:

$$J = \frac{U_\infty}{nD}, \quad Re = \frac{DU_\infty}{\nu}, \tag{1.1a,b}$$

where U_∞ is the free-stream velocity, D is the propeller disk diameter, n is the rotational speed and ν is the kinematic viscosity. The advance ratio J characterizes the relative ratio between free-stream velocity and propeller rotation. When assessing the propeller loads, thrust T is defined as the axial component of the force. The axial component of the moment of the force is the torque Q. Parameters F_H and F_V are the horizontal and vertical components of the force whose vector sum yields the total side force F_T. Non-dimensional thrust K_T, torque K_Q and side-force coefficient K_S are defined as

$$K_T = \frac{T}{\rho n^2 D^4}, \quad K_Q = \frac{Q}{\rho n^2 D^5}, \quad K_S = \frac{\sqrt{F_H^2 + F_V^2}}{\rho n^2 D^4}, \tag{1.2a–c}$$

where ρ is the fluid density, $\langle K_T \rangle$ represents the mean of the coefficient K_T and $\sigma(K_T)$ is the standard deviation. Overall, there is a lack of experimental studies of crashback. The few that do exist are of marine propeller DTMB 4381 which was studied experimentally in the David Taylor, 36-inch, variable pressure water tunnel (VPWT) for both design and crashback modes of operation for open and ducted propeller configurations (Hecker & Remmers 1971; Jiang *et al.* 1997; Jessup *et al.* 2004, 2006; Ebert, Chang & Mulvihill 2007; Swithenbank, Jessup & Etebari 2008; Donnelly, Jessup & Etebari 2010).

https://doi.org/10.1017/flo.2024.36 Published online by Cambridge University Press

Crashback has also been studied computationally. Reynolds-averaged Navier–Stokes has been used; however, it has been shown to have limitations with predicting the unsteady loads in these off-design conditions (Davoudzadeh *et al.* 1997; Chen & Stern 1999). As an alternative, hybrid methods like detached-eddy simulation and delayed detached-eddy simulation have been used (Pergande *et al.* 2017; Pontarelli, Martin & Carrica 2017). For higher fidelity, large-eddy simulation (LES) can be used to better represent unsteady flow effects and has been demonstrated to perform well in capturing the flow physics of off-design conditions like crashback. The experiments for propeller DTMB 4381 have been extensively used for LES code validation as well as propeller flow studies (Vyšohlid & Mahesh 2006; Chang *et al.* 2008; Verma, Jang & Mahesh 2012; Jang & Mahesh 2013; Kumar & Mahesh 2017; Pontarelli *et al.* 2017; Kroll *et al.* 2020; Kroll & Mahesh 2022)

For crashback of an open propeller (only the shaft and propeller without the hull of a marine vehicle), there is a significant difference between the mean experimentally measured loads $\langle K_T \rangle$ and $\langle K_Q \rangle$ of Jessup *et al.* (2004, 2006) in the VPWT and the open-water towing tank (OW) experiments by Ebert *et al.* (2007) as shown in figure 1(*a*). In addition, previous LES studying crashback (Vyšohlid & Mahesh 2006; Chang *et al.* 2008; Jang & Mahesh 2013) calculated propeller loads that significantly differed from those in the VPWT and matched closer to the OW experiments. The OW experiments did not have the influence of tunnel confinement. Jessup *et al.* (2004, 2006) acknowledged this discrepancy and hypothesized possible water tunnel interference or confinement effects due to the propeller proximity to the tunnel nozzle as well as the shear layer of the open jet as possible factors. To the authors' knowledge, there are no further detailed assessments of this discrepancy in the literature.

Water or wind tunnel test sections can provide controlled environments to study models under different conditions. The tunnel boundaries, however, can impose differences in the flow field compared with open-water conditions, giving rise to what are known as interference effects. These effects are especially strong when the model size is relatively large compared to the tunnel cross-section. When assessing the severity of interference or confinement, the blockage ratio η is used. For example, assuming a cylindrical tunnel and model shape, η is

$$\eta = \frac{A}{C}, \tag{1.3}$$

where $A = \pi R_M^2$ is the model cross-sectional area and $C = \pi R_N^2$ is the cross-sectional area of the test section. Radius R_M is the model radius and R_N is the tunnel radius. Generally, to avoid boundary interference effects, it is suggested that $\eta \ll 1$ (Glauert 1935; Barlow, Rae & Pope 1999).

There has been an extensive amount of work done on understanding interference effects and developing theoretical correction methods for symmetric solid models and bluff bodies as well as propellers in both closed- and open-test-section-type tunnels. Most of these methods were developed for wind tunnels but also apply to water tunnels. Some of the earliest contributors (Lock 1929; Glauert 1933) went as far as introducing theoretical corrections for symmetric solid models and bluff bodies based on the method of images and focused on correcting the free-stream velocity U_∞. For propellers in the design or forward mode of operation, Glauert (1933, 1935, 1947) introduced correction methods based on momentum theory and slipstream. More recent work, for example, that by Ewald (1998), Fitzgerald (2007), Werle (2011) and Segalini & Inghels (2014), built upon this foundation. However, this understanding and the correction methods built from them are limited to wind turbines and propellers operating at design conditions. For propellers in off-design conditions like crashback, these theories do not apply as the the underlying assumptions behind them fail. To the authors' knowledge, there are no studies in the current literature that examine tunnel interference or attempt to propose theoretical correction methods for propellers in crashback. This points to the complexity and challenges presented by crashback flow physics. For future experimental and computational studies of propellers in crashback, it is important to uncover the nature of water tunnel interference and obtain a clear understanding, for example, of the discrepancy between the water tunnel experiments of Jessup *et al.* (2004, 2006) and the OW experiments of Ebert *et al.* (2007).

https://doi.org/10.1017/flo.2024.36 Published online by Cambridge University Press

In this paper, LES is used to study the water tunnel interference effects of the 36-inch VPWT in crashback at $J = -0.50$ and $J = -0.82$. Some of the simulations utilize LES with an unstructured overset method. The overset methodology provides flexibility in the grid generation process, helping maintain good resolution in relevant areas like the propeller blades and body surfaces. The objectives of this study are to utilize LES to (i) identify and validate a flow physical explanation for water tunnel interference effects in crashback, (ii) offer insight to help assess the severity of their impact and (iii) demonstrate the importance of matching experimental boundary conditions for the validation of computational codes. The paper is organized as follows. The governing equations, numerical method, grid and boundary conditions and simulation set-up are described in § 2. The results are validated against experimental data in § 3 and the identified interference effects are discussed in § 4. A summary is provided in § 5.

2. Simulation details

2.1. Numerical method

The incompressible Navier–Stokes equations with an arbitrary Lagrangian–Eulerian (ALE) formulation are used. The grid velocity is included in the convection term which avoids tracking multiple reference frames for arbitrary motion of meshes. For LES, large scales are directly accounted for by the spatially filtered Navier–Stokes equations, and small scales are modelled. The filtered Navier–Stokes equations with the ALE formulation are as follows:

$$\left.\begin{aligned} \frac{\partial \bar{u}_i}{\partial t} + \frac{\partial}{\partial x_j}(\bar{u}_i\bar{u}_j - \bar{u}_i V_j) &= -\frac{\partial \bar{p}}{\partial x_i} + \nu\frac{\partial^2 \bar{u}_i}{\partial x_j \partial x_j} - \frac{\partial \tau_{ij}}{\partial x_j}, \\ \frac{\partial \bar{u}_i}{\partial x_i} &= 0, \end{aligned}\right\} \tag{2.1}$$

where u_i is the velocity in the inertial frame, p is the pressure, ν is the kinematic viscosity, V_j is the grid velocity, an overbar denotes the spatial filter and $\tau_{ij} = \overline{u_i u_j} - \bar{u}_i\bar{u}_j$ is the subgrid stress tensor. To model the subgrid stress terms, the dynamic Smagorinsky model proposed by Germano *et al.* (1991) and modified by Lilly (1992) is used. In addition, the Lagrangian time scale is dynamically computed based on a surrogate correlation of the Germano identity error (Park & Mahesh 2009). This approach has shown good performance for a variety of flows including a marine propeller in crashback (Verma & Mahesh 2012; Jang & Mahesh 2013; Kumar & Mahesh 2017, 2018*a*,*b*).

Mahesh, Constantinescu & Moin (2004) developed an unstructured numerical algorithm for LES of complex flows that emphasizes discrete kinetic energy conservation, ensuring robustness at high Reynolds numbers without numerical dissipation. This method has been successful in simulating a variety of complex marine flows (Verma *et al.* 2012; Jang & Mahesh 2013; Kumar & Mahesh 2017, 2018*b*). These previous works were performed in a non-inertial frame of reference that rotates with the propeller; this method is used for some of the simulations in this work. The other method used in the present computations is an unstructured overset grid method based on the above algorithm of Mahesh *et al.* (2004) with the capability of solving arbitrary overlapping and moving meshes (see Horne & Mahesh 2019*a*,*b*). It uses an ALE method coupled to a six-degree-of-freedom rigid-body equation system for body motion. At boundary edges of meshes, boundary conditions are obtained by performing flow-field reconstructions using overlapping meshes and geometry. This enables the use of body-fitted meshes, ensuring high resolution on the relevant geometries while aiding to save on overall mesh size and increased grid generation flexibility. In addition, this method addresses the conservation challenges of overset methods through the use of a volume-conservative super-cell interpolation. To address additional computational cost and scaling challenges of overset methods, it uses a novel communication strategy, scaling to $O(10^5)$ meshes and processors. The algorithm has been validated for a variety of problems over a range of Reynolds numbers (Kroll *et al.* 2020; Morse & Mahesh 2021; Kroll & Mahesh 2022; Morse & Mahesh 2023*a*,*b*,*c*).

https://doi.org/10.1017/flo.2024.36 Published online by Cambridge University Press

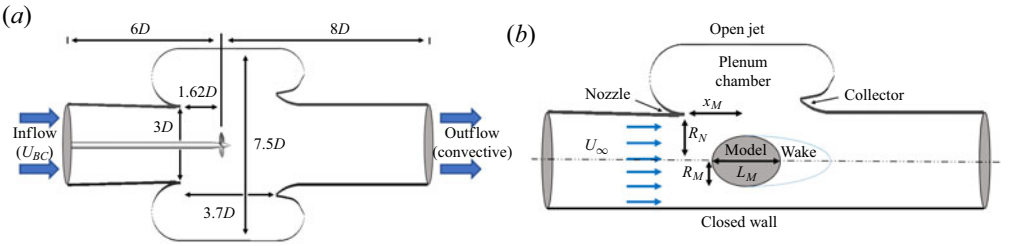

Figure 2. *(a) A cross-section of the computational domain with dimensions and boundary conditions for the VPWT with propeller DTMB 4381. The VPWT wall surface has a no-slip boundary condition. Due to the upstream, tunnel nozzle contraction, U_{BC} is set so that U_∞ is achieved at the tunnel nozzle. Diameter D is the propeller disk diameter. (b) A diagram portraying open jet (top half) and closed wall (bottom half) types of tunnels used for down-scaled model experiments with the relevant dimensions. Closed-wall tunnels have a constant cross-section wall boundary along the test section. Open-jet test sections contain a free jet and shear layer originating from the tunnel nozzle, and the boundary pressure is equal to that in the plenum chamber. Open-jet tunnels are preferred for higher-blockage-ratio models. Radius R_M is the model radius, R_N is the tunnel nozzle radius, L_M is the model length, x_M is the distance to the model and U_∞ is the free-stream velocity.*

2.2. Problem description, geometry and computational mesh

Open propeller (only shaft and propeller without the hull of a marine vehicle) crashback experiments were performed in the David Taylor, 36-inch VPWT (Jessup *et al.* 2004, 2006). Figure 2(*a*) shows a cross-section of the VPWT, a cylindrical, open-jet-type water tunnel, and figure 2(*b*) describes the different type of tunnels used in experiments. According to Glauert (1933), open-jet-type tunnels help attain open-water conditions at higher blockage ratios (up to $\eta = 0.6$–0.7). These experiments used the down-scaled propeller model DTMB 4381, a five-bladed, right-handed propeller with variable pitch, and no skew or rake with a diameter $D = 12.0$ inches. More details of the 36-inch VPWT geometry and propeller model DTMB 4381 are provided in Jessup *et al.* (2004, 2006), Swithenbank *et al.* (2008) and Donnelly *et al.* (2010). The LES performed in this study attempt to replicate these experiments for validation and insight into water tunnel interference effects in crashback at $J = -0.50$ and $J = -0.82$.

For comparison, LES of this same propeller in open-water conditions are also conducted to match and validate against the OW experiments by Ebert *et al.* (2007). These experiments better represented open-water or unconfined conditions. For mesh generation, computer-aided design models of the propeller model DTMB 4381 and the 36-inch VPWT were utilized with the mesh generation software Pointwise (Cadence) and GridPro.

2.2.1. The 36-inch VPWT

First, the 36-inch VPWT geometry without the propeller model is simulated at Reynolds number $Re = 561\,000$, based on the propeller diameter D. This simulation is used to assess the best grid resolution and provide some insight into the flow characteristics of the water tunnel without a model inside. Figure 2(*a*) provides a cross-section of the VPWT, the geometric dimensions and the boundary conditions for the case set-up with the propeller model. The domain inflow is $6D$ upstream of the propeller origin or centre. Here, the inflow boundary condition U_{BC} is set. In the experiments, U_∞ is determined using the mean measured bulk flow at specific cross-sections where the cross-sectional areas are estimated, and pressure taps provide pressure measurements (Jessup *et al.* 2004). The free-stream velocity U_∞ at the tunnel nozzle then remains constant into the open-jet test section. For the simulations, the continuity equation is used to calculate U_{BC} that leads to the desired U_∞ at the tunnel nozzle. The cross-sectional areas are approximated at the domain inflow location (using the diameter $D_{in} = 3.23D$) and at the tunnel nozzle (using the diameter $D_N = 3D$). A convective boundary condition is set at the

https://doi.org/10.1017/flo.2024.36 Published online by Cambridge University Press

Table 1. *The grid information for the empty 36-inch VPWT geometry, the crashback $J = -0.82$ and $J = -0.50$ cases with (VPWT) and without (OW) the VPWT geometry. Here CVs is the number of control volumes and Procs is the number of processors that the grid was partitioned. The OW simulations used two grids: the first is a background and the other an overset mesh.*

Grid	CVs ($\times 10^6$)	Procs
Empty VPWT	17.6	352
P4381 VPWT	45.0	928
P4381 OW	8.9 (5.2 + 3.7)	576 (336 + 240)

domain outlet, which is located at $8D$ downstream of the propeller centre. A no-slip boundary condition is set at all wall surfaces with a minimum wall-normal spacing of $0.0017D$ with a growth ratio of 1.01. The non-dimensional time step is $\Delta t U_\infty / D = 1.667 \times 10^{-4}$ and a total simulation time equivalent to nine full domain flow passes was simulated. Due to computational cost, a single grid is used. More grid information is provided in table 1. The 36-inch VPWT grid is later used as the background grid for the propeller cases.

2.2.2. Crashback for propeller DTMB 4381

Crashback cases provide many challenges, one of the most important being the computational cost. This flow is unsteady with unpredictable low-frequency fluctuations of the vortex ring that impact the loads (Jang & Mahesh 2013). Large-eddy simulation helps capture the unsteady flow features but at a greater computational expense. In addition, the simulation run time must be long enough to ensure statistical convergence of flow parameters and the loads, requiring hundreds of revolutions. For this reason, this work focuses on assessing interference effects at only two advance ratios of $J = -0.50$ and $J = -0.82$. These are at the different ends of the advance ratio range shown in figure 1(*a*). They are selected to capture the interference effects responsible for the larger difference in the loads at high $|J|$ (magnitude of J) and the decrease of this difference at lower $|J|$. To identify and study potential water tunnel interference effects in the crashback mode of operation, the flow is simulated at Reynolds number $Re = 561\,000$ and advance ratios of $J = -0.50$ and $J = -0.82$ with the VPWT geometry included. In addition, to further reduce the computational cost, a single-grid approach is used as the Navier–Stokes equations are solved in the rotating reference frame similar to that done by Vyšohlid & Mahesh (2006), Chang *et al.* (2008), Verma *et al.* (2012), Jang & Mahesh (2013) and Kumar & Mahesh (2017). The empty VPWT grid used in § 2.2.1 is edited to include the hub and propeller DTMB 4381 to form one single grid. The propeller is rotated at rotational velocity $\omega = 2\pi n$ to match the advance ratio. It is important to note that the propeller rotation rate determined by J is the same for the VPWT and OW cases. No-slip boundary conditions are set on the VPWT wall surfaces and the hub. On the blade mesh surfaces and parts of the hub surface, $v = \omega \times r$ boundary conditions are set, where ω matches the advance ratio J. The domain and boundary conditions are shown in figure 2(*a*). A pill-box of tetrahedral cells is used around the blade, similar to previous LES by Chang *et al.* (2008), Verma *et al.* (2012), Jang & Mahesh (2013) and Kroll *et al.* (2020). On the blade surface, four prism layers are extruded at a height of $0.0017D$ and a growth ratio of 1.01. On all other surfaces, the minimum wall-normal spacing is the same as on the blades. It is also important to mention that resolving the attached boundary layer is not required to make accurate predictions due to the separated nature of crashback flow (Jang & Mahesh 2013). Additional information on the size and partitioning of the meshes is presented in table 1.

In addition to the two cases aforementioned with the VPWT geometry, two additional cases are simulated in open-water or unconfined conditions to compare and contrast. The cases are simulated at Reynolds number $Re = 480\,000$ and advance ratios of $J = -0.50$ and $J = -0.82$. The overset methodology is used with a total of two grids in the simulation. The background grid is a fully cylindrical grid with the same axial dimensions as for the VPWT case but a constant cross-sectional diameter of $7D$, similar to the previous LES (Chang *et al.* 2008; Verma *et al.* 2012; Jang & Mahesh 2013;

https://doi.org/10.1017/flo.2024.36 Published online by Cambridge University Press

Table 2. *A summary of the LES cases simulated in this study. Case P4381 OW is the unconfined case without the 36-inch VPWT geometry.*

	Empty VPWT	P4381 VPWT	P4381 VPWT	P4381 OW	P4381 OW
J	—	−0.82	−0.50	−0.82	−0.50
Re	561 000	561 000	561 000	480 000	480 000
Run time (hours per rev.)	—	8.2	5	2.73	1.66
Total time (days)	0.73	68.33	41.67	22.75	13.83

Kroll *et al.* 2020) where it was shown to better represent open-water conditions. A far-field boundary condition of U_∞ is enforced at the radial domain edge. This grid also contains most of the propeller hub geometry. An overset grid contains all five blades of propeller DTMB 4381 and the rest of the hub. The background mesh is generated with a cylindrical cut to remove redundant control volumes with enough overlap between the meshes for viable interpolation partner pairs. The overset mesh also utilizes a pill-box of tetrahedral cells in the near-blade areas with blade and hub wall resolutions similar to those of the VPWT crashback cases. Further details can be found in the validation work by Kroll *et al.* (2020). Table 1 presents more information on the size and partitioning of the mesh.

All crashback simulations are run for over 200 revolutions, with a minimum of 150 revolutions of phase-averaged flow-field statistics collected to ensure statistical convergence of the flow field and the unsteady loads. The computational time step used for the $J = -0.50$ cases is $\Delta t U_\infty/D = 1.667 \times 10^{-4}$, which corresponds to a propeller rotation of 0.1200° per time step. The computational time step used for the $J = -0.82$ cases is $\Delta t U_\infty/D = 1.667 \times 10^{-4}$, which corresponds to a propeller rotation of 0.0857° per time step. According to the experimental observations of Jessup *et al.* (2004), the force coefficients in crashback do not vary with Reynolds number in the range $4 \times 10^5 < Re < 9 \times 10^5$. Table 2 summarizes the parameters for the five LES cases in this work, which required considerable computational effort due to the statistical convergence required for the crashback cases.

3. Validation

3.1. The 36-inch VPWT

Contour slices of axial velocity and the pressure coefficient for the empty VPWT are shown in figure 3. The pressure coefficient is defined as

$$C_p = \frac{p - p_\infty}{\frac{1}{2}\rho U_\infty^2}, \tag{3.1}$$

where p_∞ is the reference pressure. The flow is accelerated through the VPWT contraction and into the test section where the desired mean bulk flow U_∞ is achieved. This is confirmed by integrating the velocity profile at the tunnel nozzle. Velocity U_∞ is maintained at the tunnel nozzle and into the open-jet section, providing a designed, controlled environment for the model propeller tests (figure 3*a*,*c*). Flow from the tunnel nozzle interacts with the plenum chamber, forming a free-shear layer (jet-shear layer) that grows in thickness downstream (figure 3*a*,*c*). Unsteadiness is introduced into the flow, as vortices are formed due to the aforementioned interaction (figure 3*b*). Downstream, flow collides with the collector section, characterized by the higher-pressure section in figure 3(*b*,*d*). Some flow spills into the plenum chamber while most of it is funnelled out of the test section.

3.2. Crashback ($J = -0.82$ and $J = -0.50$)

The K_T and K_Q propeller load statistics between VPWT and OW experiments show a significant discrepancy (figure 1*a*). This difference manifests as a reduction in the magnitude of the force coefficients

https://doi.org/10.1017/flo.2024.36 Published online by Cambridge University Press

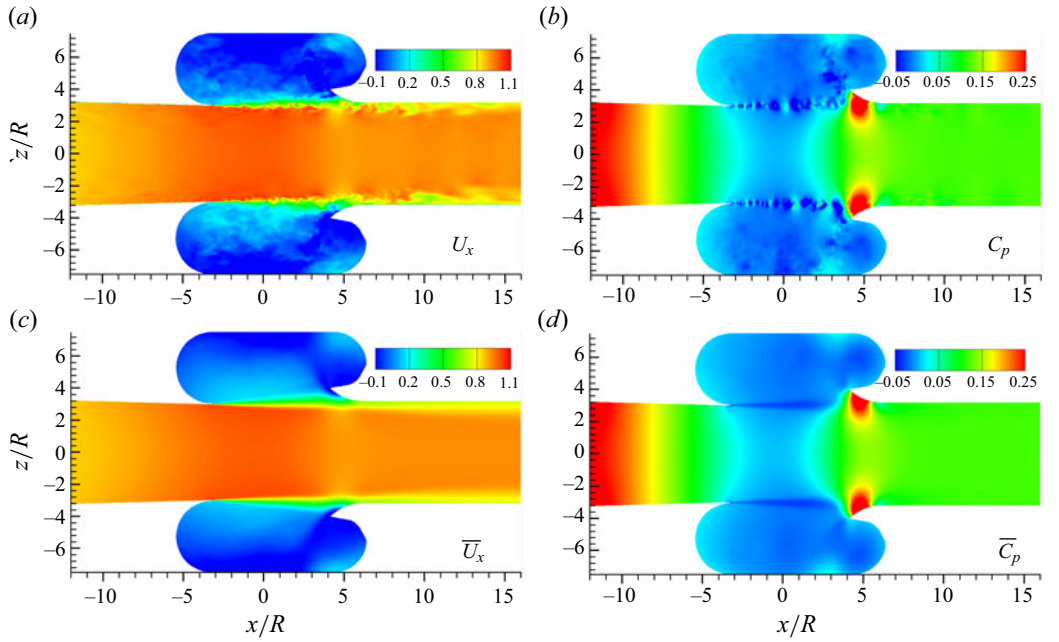

Figure 3. *Constant y-plane ($y = 0$) contours of (a) instantaneous axial velocity U_x, (b) instantaneous pressure coefficient C_p, (c) mean axial velocity $\bar{U}_x$ and (d) mean pressure coefficient $\bar{C}_p$. Radius $R = D/2$ is the propeller disk radius. The flow-field quantities are normalized appropriately using ρ and U_∞.*

Table 3. *Crashback ($J = -0.70$). A comparison of load statistics: LES-1 (Jang & Mahesh 2013), LES-2 (Kroll et al. 2020), VPWT (Jessup et al. 2004) and OW (Ebert et al. 2007). Here LES-1 and LES-2 use the unconfined domain of diameter 7D. Note that, unfortunately, the OW data do not include higher-order statistics.*

	LES-1 (coarse)	LES-1 (fine)	LES-2	VPWT	OW
$\langle K_T \rangle$	−0.39	−0.38	−0.41	−0.33	−0.41
$\sigma(K_T)$	0.0620	0.0550	0.0520	0.0600	—
$\langle K_Q \rangle$	−0.078	−0.074	−0.081	−0.065	−0.078
$\sigma(K_Q)$	0.0120	0.0100	0.0100	0.0110	—
$\langle K_S \rangle$	0.035	0.027	0.029	0.030	—

K_T and K_Q for the VPWT data compared with the OW data. The load statistics for $J = -0.7$ presented in table 3 reveal that the discrepancy between VPWT experiments also exists with previous LES of Jang & Mahesh (2013) and Kroll *et al.* (2020). In fact, these LES used a constant cylindrical domain of diameter $7D$ to better represent open-water conditions and better matched the OW experiments.

The present LES loads in table 4 show that for $J = -0.82$ there is a significant discrepancy between the VPWT and OW experimental data with up to a 30 % difference, demonstrating the large impact of the interference effects. The VPWT loads are of a lower magnitude compared with OW. This discrepancy is maintained between the simulation results as well. The LES VPWT load statistics presented in table 4 compare well with the VPWT experiments as mean K_T and K_Q are within 5 % of the VPWT experimental data. The standard deviations of K_T and K_Q and the side force K_S are also in good agreement. The unconfined (LES OW) load statistics also compare well with mean K_T and K_Q within 5 % of the OW

https://doi.org/10.1017/flo.2024.36 Published online by Cambridge University Press

Table 4. *Crashback ($J = -0.82$). A comparison of load statistics: LES VPWT (the current simulation), VPWT (Jessup et al. 2004), LES OW (the current unconfined simulation) and OW (Ebert et al. 2007). Note that the experimental values were specifically for $J = -0.80$.*

	LES VPWT	VPWT	LES OW	OW
$\langle K_T \rangle$	−0.39	−0.37	−0.52	−0.52
$\sigma(K_T)$	0.056	0.057	0.0904	—
$\langle K_Q \rangle$	−0.076	−0.076	−0.100	−0.096
$\sigma(K_Q)$	0.011	0.010	0.0165	—
$\langle K_S \rangle$	0.028	0.032	0.050	—

Table 5. *Crashback ($J = -0.50$). A comparison of load statistics: LES VPWT (the current simulation), VPWT (Jessup et al. 2004), LES OW (the current unconfined simulation), LES-1 (Chang et al. 2008) and OW (Ebert et al. 2007). Here LES-1 uses the unconfined domain of diameter 7D.*

	LES VPWT	VPWT (1)	VPWT (2)	LES OW	LES-1	OW
$\langle K_T \rangle$	−0.30	−0.27	−0.29	−0.32	−0.34	−0.32
$\sigma(K_T)$	0.0583	0.0560	0.0440	0.0587	0.0560	—
$\langle K_Q \rangle$	−0.059	−0.057	−0.054	−0.065	−0.064	−0.068
$\sigma(K_Q)$	0.0115	0.0110	0.0083	0.0113	0.0100	—
$\langle K_S \rangle$	0.025	0.031	0.029	0.025	0.025	—

experimental data. Unfortunately, data for the standard deviations and side force are not available to compare.

Table 5 shows load data for $J = -0.50$ for the VPWT and OW LES cases in comparison with the experimental VPWT and OW data. The discrepancy observed for mean K_T and K_Q between the VPWT and OW experimental data still exists, though the overall magnitude of the difference is smaller compared with the $J = -0.82$ case. This implies weaker or reduced interference effects on U_∞ for this J. The VPWT experimental load data show an appreciable amount of scatter (Jessup *et al.* 2004, 2006). The LES VPWT loads presented in table 5 are within the scatter of the VPWT experimental data with good agreement also for the higher-order statistics $\sigma(K_T)$ and $\sigma(K_Q)$ and the side force K_S. The unconfined (LES OW) mean K_T and K_Q values match within 6 % those of the OW experiments.

These results partnered with those of the $J = -0.82$ case add confidence in the use of LES to capture crashback flow with the different domain boundary conditions, as the loads compare well with their corresponding setting. In addition, we can now confirm the substantial effect that the VPWT geometry has on the load statistics. Altogether, this is initial evidence that when comparing with the experiments of Jessup *et al.* (2004, 2006), it is very important that the VPWT geometry is included in any simulations to match the experimental boundary conditions and validate the results.

4. Results

4.1. Interference effects in crashback

The following sections detail the flow physics of interference effects for a propeller in crashback. Before analysing the results in the coming sections, we can hypothesize on what to expect using current knowledge of fluid dynamics and crashback flow physics. Afterwards, we attempt to support this with evidence from the simulation results.

https://doi.org/10.1017/flo.2024.36 Published online by Cambridge University Press

As discussed by Lock (1929) and Glauert (1933, 1935, 1947), tunnel interference effects affect the magnitude of the experimental free-stream velocity U_∞. Therefore, the interference effects identified in propeller crashback affect the local U_∞ experienced by the propeller and therefore the advance ratio J. This implies that the flow physics under interference effects should resemble a different J from that set-up. A consequence of this is that the loads would also resemble those of a different J. Previous work on propeller crashback, especially that of Jang & Mahesh (2013), identified the various flow physical changes that occur due to varying the advance ratio J. One of the most consequential concerns the vortex ring diameter which increases with increasing $|J|$ and another is the increase in the strength of the jet-like, propeller-induced reverse flow with decreasing $|J|$.

Jang & Mahesh (2013) also identified that for larger magnitudes of the advance ratio ($J < -0.50$), the greater free-stream velocity magnitude dominates the effects of the propeller rotation and propeller-induced reverse flow, leading to greater magnitudes of the propeller loads as they scale with ρU_∞^2. For lower magnitudes of the advance ratio ($J > -0.50$), the propeller rotation rate is large and the propeller-induced reverse flow is strong enough to create local blade flow similar to a steady backing condition, as the loads then scale with $\rho n^2 D^2$. This partnered with the effect on U_∞ implies that interference effects have a greater impact for higher-$|J|$ cases while weakening for low-$|J|$ cases.

In crashback, the vortex ring is formed by the free-stream flow interaction with the propeller-induced reverse flow. The vortex ring redirects flow around it while simultaneously trapping a volume of fluid that recirculates about its centre. This displaces the flow inside the water tunnel similar to the case of the presence of a solid model. This implies that the vortex ring impact on the flow field in crashback resembles that of a solid model or bluff body in uniform flow. To add to this, the propeller-induced reverse flow pushes the flow region of influence further upstream of the propeller and thus can contribute more to the volume displacement. Therefore, the observed interference effects should resemble those that affect solid models. The impact of these flow features also has implications for assessing the severity of interference using the blockage ratio η.

4.2. Flow field: crashback ($J = -0.82$ and $J = -0.50$)

The $J = -0.82$ case is in a range where the free-stream strength dominates the propeller-induced reverse flow. Interference effects that affect U_∞ should therefore be stronger in this regime. A comparison of the instantaneous and mean axial velocity contours of the VPWT and OW LES in figure 4 reveals some substantial differences in the flow field. In figure 4(*a*,*c*), the propeller-induced reverse flow in the VPWT is strong enough to slow the incoming upstream flow near the tunnel nozzle. The unsteady vortex ring appears to be restricted to lie within the confines of the jet shear layer. It is responsible for redirecting some flow into the plenum chamber of the open-jet section, destabilizing and deforming the jet shear layer. The flow that does move downstream of the propeller is mostly suctioned into the outlet; however, some flow is deflected by the collector section and into the plenum chamber. The vortex ring and jet shear layer interaction form a mean convex interface within the plenum chamber of the VPWT (figure 4*c*). Instantaneously, this boundary deforms and moves according to the vortex ring and jet shear layer interaction, as seen in figure 4(*a*). The wake formed from these complex interactions extends into the collector section as flow is funnelled out. Figure 1(*b*) encapsulates these aforementioned instantaneous flow characteristics. In figure 4(*b*,*d*), the OW case reveals a flow that is less restricted due to a larger domain diameter. At the propeller centre, the flow approaches U_∞ further away radially. The blockage ratio using the propeller diameter is $\eta = 0.01$ which suggests that numerical blockage should be negligible. This is confirmed by the validation of previous LES studies that used the same domain size (Chang *et al.* 2008; Verma *et al.* 2012; Jang & Mahesh 2013; Kroll *et al.* 2020) and the load statistics from the present cases.

The $J = -0.50$ case is in a range where the propeller-induced reverse flow and propeller rotation dominate over the strength of the free stream. Interference effects that affect U_∞ would not be expected to be as strong. A comparison of the instantaneous and mean axial velocity contours of the VPWT in

https://doi.org/10.1017/flo.2024.36 Published online by Cambridge University Press

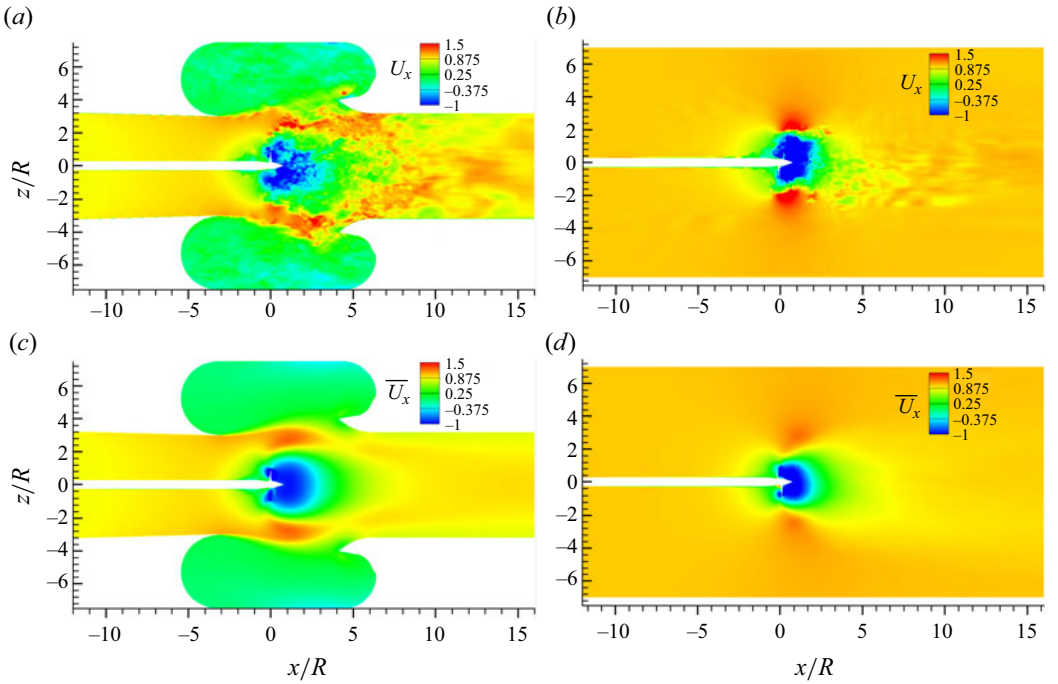

Figure 4. *Crashback ($J = -0.82$) VPWT: constant y-plane ($y = 0$) contours of (a) instantaneous axial velocity U_x and (c) mean axial velocity $\bar{U}_x$. Crashback ($J = -0.82$) OW: contours of (b) instantaneous axial velocity U_x and (d) mean axial velocity $\bar{U}_x$. The flow-field quantities are normalized with U_∞.*

figure 5 reveals a flow field with similar characteristics to those of the $J = -0.82$ case. Most noticeable is the mean convex interface into the plenum chamber of the VPWT (figure 5*c*). Interestingly, the instantaneous axial velocity contours in figure 5(*a*) reveal a strong axial jet of reverse flow that reaches the upstream tunnel nozzle. As characterized by Chang *et al.* (2008), the propeller reverse flow in crashback at this range of J was shown to have modes of behaviour similar to an axial jet as observed here. In figure 5(*b*,*d*), the OW case exhibits a flow that is less confined as the flow above the propeller plane is not accelerated to the same extent as in the VPWT. At the propeller centre, the flow approaches U_∞ further away radially. Like the $J = -0.82$ case, numerical blockage is negligible. Interestingly, the propeller-induced reverse flow appears to be weaker for the OW case than for the VPWT, a sign that interference effects have an appreciable impact on the flow.

4.3. Interference effects in crashback: vortex ring and axial jet of reverse flow

The most important flow feature in crashback, Jang & Mahesh (2013) characterized the vortex ring as highly unsteady and unpredictable as it often breaks up and sheds, contributing to highly unsteady loads. In the VPWT LES, we can observe complex instantaneous flow interactions as a broken-down vortex ring interacts with the jet shear layer in the VPWT, pushing flow into the plenum chamber (figures 1*b*, 4*a* and 5*a*). Identification of the relationship of the vortex ring to interference effects using the instantaneous flow field is a challenge. However, the mean flow statistics can help uncover its role.

First, we can characterize the mean vortex ring impact on the flow field in crashback as that of a solid model or bluff body in uniform flow. The characteristics of the mean flow field support this, with the following being the evidence. In the upstream region, the propeller-induced reverse flow collides with the free-stream flow forming a stagnation region, similar to the effect due to the presence of a solid model. This can be observed for all cases as the low-velocity-magnitude region in figure 6. This then

https://doi.org/10.1017/flo.2024.36 Published online by Cambridge University Press

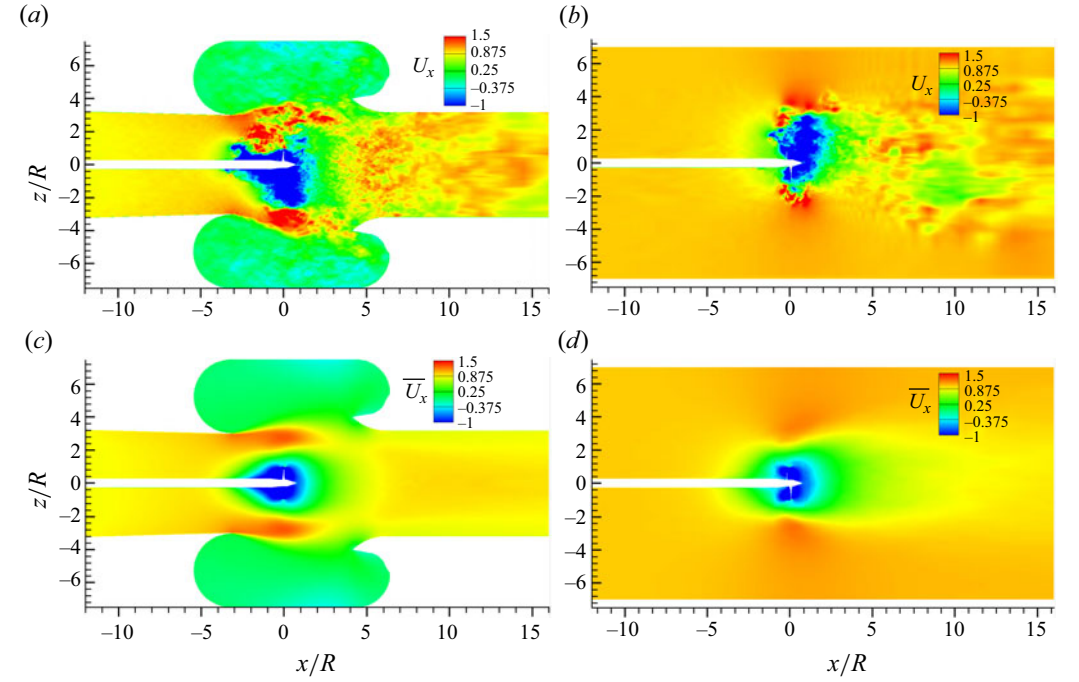

Figure 5. *Crashback ($J = -0.50$) VPWT: constant y-plane ($y = 0$) contours of (a) instantaneous axial velocity U_x and (c) mean axial velocity $\bar{U}_x$. Crashback ($J = -0.50$) OW: contours of (b) instantaneous axial velocity U_x and (d) mean axial velocity $\bar{U}_x$. The flow-field quantities are normalized with U_∞.*

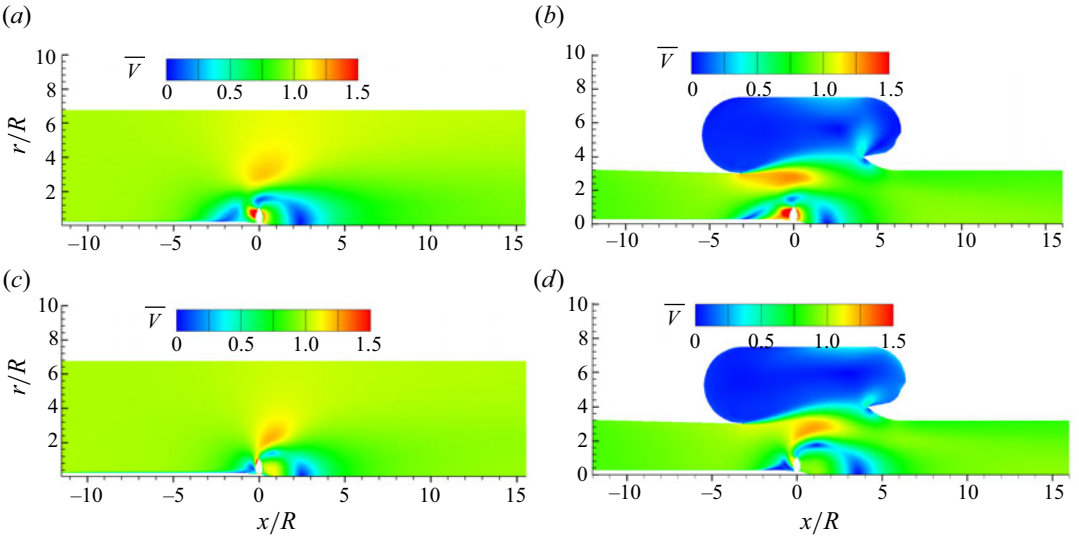

Figure 6. *Contours of mean velocity magnitude $\overline{V}$ for (a) $J = -0.50$ OW, (b) $J = -0.50$ VPWT, (c) $J = -0.82$ OW and (d) $J = -0.82$ VPWT cases. The flow-field quantities are normalized with U_∞.*

https://doi.org/10.1017/flo.2024.36 Published online by Cambridge University Press

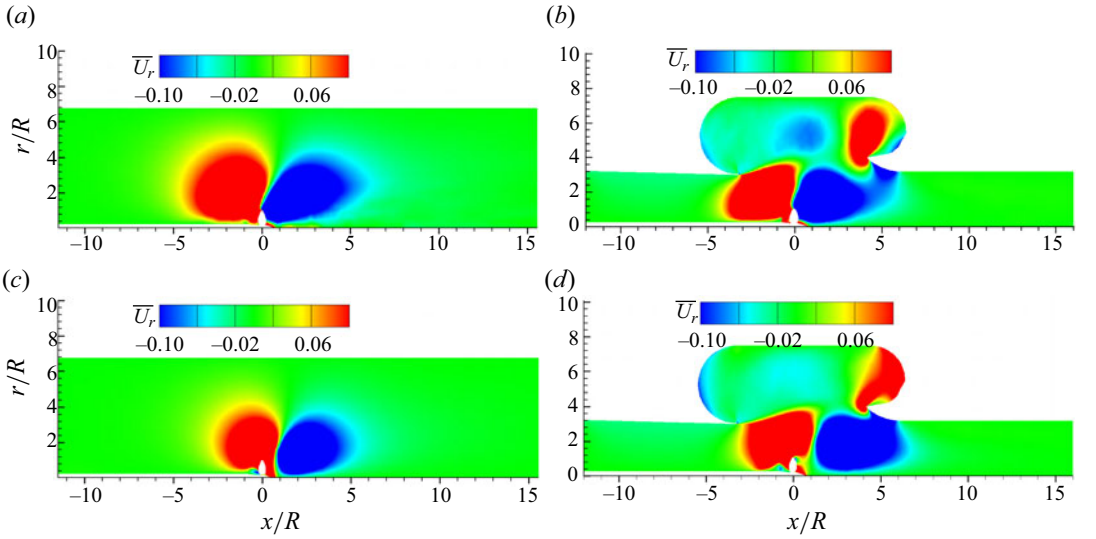

Figure 7. *Contours of mean radial velocity $\bar{U}_r$ for (a) $J = -0.50$ OW, (b) $J = -0.50$ VPWT, (c) $J = -0.82$ OW and (d) $J = -0.82$ VPWT cases. The flow-field quantities are normalized with U_∞. Note that the magnitude range used in the legend is small to exaggerate the differences.*

leads to the redirecting of flow radially outwards (radially positive) and around the propeller. Figure 7 shows that a large region around the propeller experiences an induced positive, radial velocity and then that component switches direction downstream past the propeller plane, forming the vortex ring. Downstream of the propeller plane, there is another stagnation region (figure 6). This represents the boundary between the reverse flow and the free-stream flow that flows past the vortex ring, almost like the boundary of a solid model.

Further evidence of the solid model characteristics of the flow field around the vortex ring arises in the circumferentially averaged pressure field. An adverse pressure gradient is formed upstream of the vortex ring as the free-stream flow collides with the propeller-induced reverse flow (figure 8), then this pressure gradient flips direction around the vortex ring, and flips direction once more as flow moves downstream in the wake. This pressure field closely resembles that around a circular cylinder in uniform flow, which has been studied extensively (e.g. Roshko 1961). To summarize the overall effect of the vortex ring, figure 9(*a*,*b*) shows the circumferentially averaged mean pressure coefficient $\bar{C}_p$ with streamlines for the $J = -0.50$ and $J = -0.82$ cases in the VPWT. As flow approaches the vortex ring it is slowed down and redirected to move around the vortex ring where the streamlines contract, with a corresponding acceleration of the flow due to the decreasing pressure. Downstream, the streamlines expand and corresponding deceleration of flow occurs. Starting from the upstream stagnation point to the downstream one, a streamline can be traced that separates the recirculating volume of fluid from the flow that goes around the vortex ring. Tracking $\bar{C}_p$ on this streamline, we find that this distribution qualitatively resembles that around the surface of a circular cylinder in uniform flow (figure 9*c*). This is characterized by an initial high $\bar{C}_p$ that reduces to a minimum and then starts increasing again, the same effect as that of a solid model. In crashback, however, this is caused by the trapped recirculating volume that flow has to go around. Instantaneously, the quantity of this volume fluctuates with the characteristics of the vortex ring (its size and stability), which are dependent on the advance ratio J.

It is also important to point out the impact of propeller reverse flow. Its effects are most consequential for the case of lower magnitude of J ($J = -0.50$). In this range of J, the propeller reverse flow behaves like an axial jet (Chang *et al.* 2008) and can be strong enough to approach the tunnel nozzle (figure 5*a*,*c*). The outcome is that the propeller-induced reverse flow pushes the stagnation zone into the tunnel nozzle, also extending the pressure field (figures 8*b* and 9*a*) and adding to the volume displacement.

https://doi.org/10.1017/flo.2024.36 Published online by Cambridge University Press

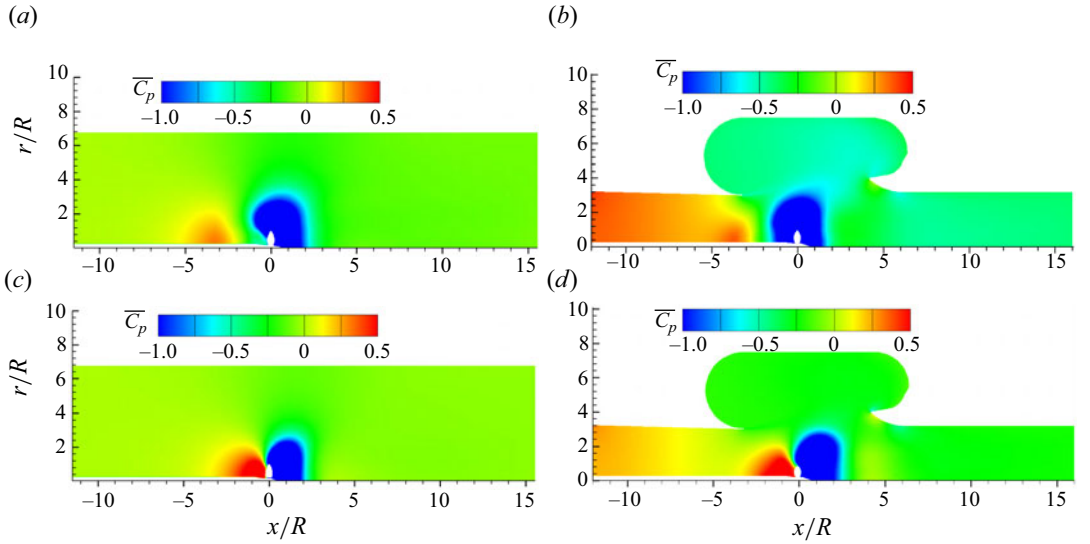

Figure 8. *Contours of the mean pressure coefficient $\bar{C}_p$ for (a) $J = -0.50$ OW, (b) $J = -0.50$ VPWT, (c) $J = -0.82$ OW and (d) $J = -0.82$ VPWT cases. The flow-field quantities are normalized appropriately using ρ and U_∞.*

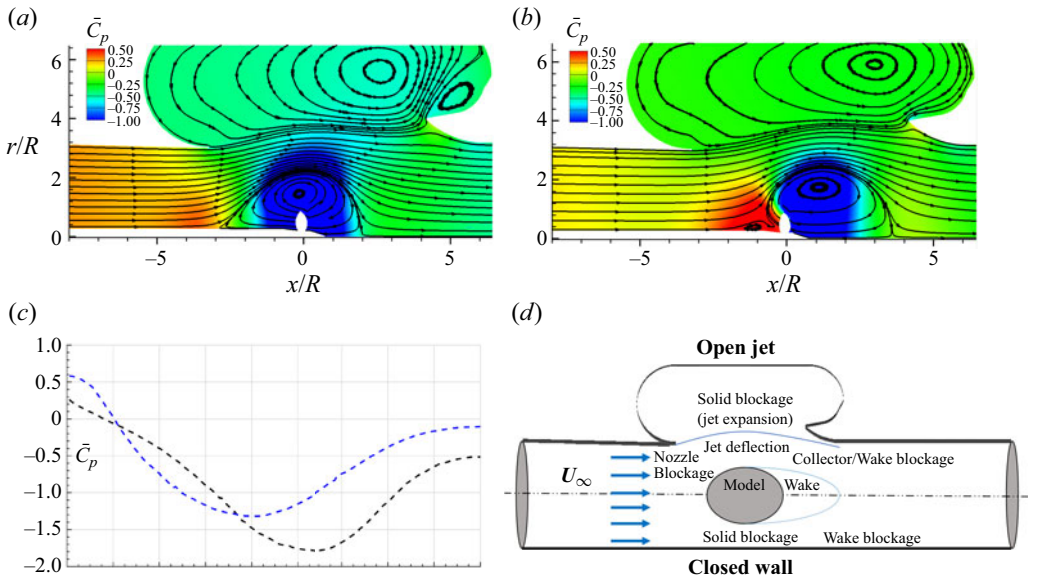

Figure 9. *Circumferentially averaged contours of mean pressure coefficient $\bar{C}_p$ with streamlines for (a) $J = -0.50$ VPWT and (b) $J = -0.82$ VPWT. (c) Coefficient $\bar{C}_p$ along a streamline starting from the upstream stagnation point to the downstream one, for $J = -0.50$ VPWT (black) and $J = -0.82$ VPWT (blue). (d) A diagram summarizing the interference effects for open jet (top half) and closed wall (bottom half) types of tunnels used for down-scaled model experiments. The flow-field quantities are normalized appropriately using ρ and U_∞.*

https://doi.org/10.1017/flo.2024.36 Published online by Cambridge University Press

Table 6. *Parameters are taken at various axial locations upstream of the propeller. First, the estimated cross-sectional (C-S) radii of the edge of the jet shear layer for the VPWT $J = -0.50$ and $J = -0.82$ cases. Then the cross-sectional area ratios A_{j5}/A_{j8} between the VPWT $J = -0.50$ and $J = -0.82$ cases. Next, a comparison of ratios of the integrated mean axial velocity (VPWT/OW) at various upstream, axial locations for both cases. Here SL is integrated from the hub to the edge of the jet shear layer while PP is integrated to the edge of the propeller plane ($r/R = 1$). Location $x/R = -3.24$ is the tunnel nozzle location with a radius $r/R = 3.00$ and $x/R = 0.00$ is the propeller location.*

Axial location: x/R	−3.24	−3.00	−2.00	−1.00	0.00	1.00
$J = -0.50$: C-S, r/R	3.00	3.00	3.10	3.24	3.32	3.20
$J = -0.82$: C-S, r/R	3.00	2.98	2.99	3.10	3.30	3.42
C-S ratio: A_{j5}/A_{j8}	1.00	1.01	1.07	1.09	1.01	0.8781
$J = -0.50$: PP:U_{wt}/U_{op}	0.93	0.86	−0.68	2.50	—	—
$J = -0.82$: PP:U_{wt}/U_{op}	1.01	1.00	0.89	0.44	—	—
$J = -0.50$: SL:U_{wt}/U_{op}	1.07	1.07	1.012	0.89	—	—
$J = -0.82$: SL:U_{wt}/U_{op}	1.01	1.01	0.98	0.86	—	—

4.4. Interference effects in crashback: solid blockage (jet expansion)

As described in the previous section, in the VPWT, an open-jet tunnel, the mean vortex ring recirculation has a similar effect to that of a solid model or bluff body. Therefore, the interference effects experienced by a propeller in crashback should resemble those of a solid model (figure 9*d*) (see Glauert (1933, 1935), Cooper (1998), Krynytzky & Ewald (1998), Mercker (2013), Wickern (2014) and Collin *et al.* (2016) for further details). The main interference effect experienced by solid models in open or closed tunnels is called solid blockage and is caused by the displacement of the model volume inside the tunnel. In closed tunnels, it occurs when the cross-sectional area between the model and the tunnel is restricted. The continuity effect due to mass conservation increases the flow velocity, to counter the reduced cross-sectional area. For open-jet tunnels, the continuity effect has the opposite effect, decreasing the flow velocity, and is referred to as the jet expansion effect (Glauert 1933, 1935). In this section, we examine the evidence demonstrating that a propeller in crashback experiences solid blockage.

The solid blockage effect is characterized by the expansion of the jet shear-layer boundary. This causes a curvature of the interface between the jet shear layer and the plenum chamber, as seen in figures 4(*c*) and 5(*c*). Flow moves further radially into the plenum chamber than in the case of the empty VPWT (figure 3*a*,*b*). The streamlines at the interface (figure 9*a*,*b*) show evidence of the curvature which extends past the tunnel nozzle radius ($r/R = 3$). For further evidence of this, the cross-sectional radii representative of the jet boundary at various axial (x/R) locations are estimated. The edge of the jet shear layer is estimated as the radial location where the mean axial velocity magnitude reduces below U_∞. The cross-sectional radii are presented in table 6, where they increase further downstream for both cases with the $J = -0.82$ case hitting a higher peak.

The jet expansion effect also reduces the free-stream velocity experienced by a solid model in an open-jet water tunnel. Evidence of this in the VPWT is in figure 10(*a*,*b*), the profiles of mean axial velocity at various stations, comparing the $J = -0.50$ and $J = -0.82$ VPWT and OW cases. For the same J, the VPWT cases reveal a mean velocity deficit upstream of the propeller ($x/R < 0$) and in the propeller plane ($r/R < 1$) when compared with the OW case. To further clarify, the propeller plane mean axial velocity magnitudes can be estimated by radial integration from the hub surface to the propeller radius $r/R = 1$ at various axial locations. Presented in table 6 are the ratios of these velocities between the VPWT and OW cases (PP:U_{wt}/U_{op}). It also appears that flow is accelerated above the propeller plane ($r/R > 1$). To better clarify the overall effect of solid blockage interference, the mean axial velocity magnitude is also radially integrated from the hub surface to the edge of the jet shear layer at various axial locations. Also presented in table 6 are the ratios of these velocities between the VPWT and

https://doi.org/10.1017/flo.2024.36 Published online by Cambridge University Press

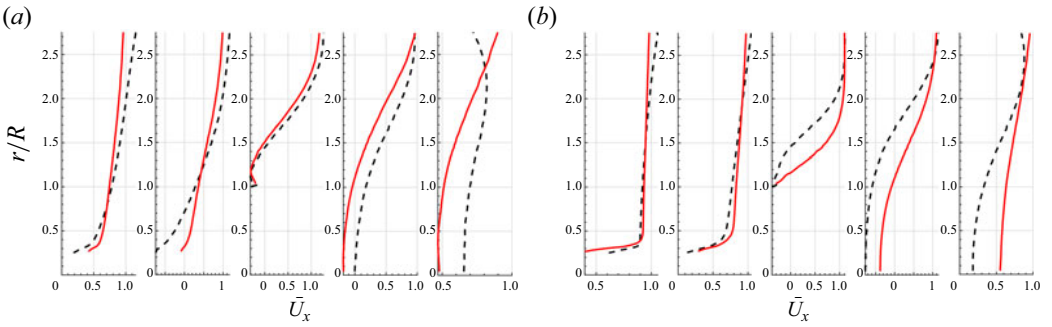

Figure 10. *Circumferentially averaged profiles of the mean axial velocity $\bar{U}_x$ at various axial locations for (a) $J = -0.50$ and (b) $J = -0.82$; dashed lines are the VPWT result and solid lines are the OW result. In each panel, the locations are from left to right $x/R = -3.23$, $x/R = -2.00$, $x/R = 0.00$, $x/R = 2.00$ and $x/R = 4.00$. The propeller is located at $x/R = 0.00$. The flow-field quantities are normalized with U_∞.*

OW cases (SL:U_{wt}/U_{op}) which confirm the deficit introduced by solid blockage (see $x/R = -2.00$ and $x/R = -1.00$). Overall, solid blockage is confirmed with the jet expansion effect increasing the cross-sectional area of flow in the tunnel which then causes a reduction in the mean axial velocity magnitude experienced by the propeller as a result of the continuity effect.

4.5. Interference effects in crashback: nozzle blockage

Another important interference effect experienced by solid models is specific to open-jet tunnels and is referred to as nozzle blockage (figure 9*d*). In this section, we examine the evidence demonstrating that in an open-jet water tunnel like the VPWT, a propeller in crashback experiences nozzle blockage. This effect occurs due to a solid model's proximity to the tunnel nozzle (Mercker, Wickern & Wiedemann 1997; Wickern 2001; Mokhtar & Britcher 2008). The pressure field induced by the model extends into the tunnel nozzle and creates an effect similar to solid blockage in a closed-section tunnel. Therefore, this effect is characterized by an increase in the magnitude of the free-stream velocity, the opposite of the effect of jet expansion.

We have shown that the vortex ring partnered with the propeller-induced reverse flow penetrates the tunnel nozzle (§ 4.3). The impact of this adverse pressure gradient is the displacement and acceleration of the free-stream flow near the tunnel nozzle, especially above the propeller plane $r/R > 1$ (figures 4*c* and 5*c*). The profiles at the tunnel nozzle ($x/R = -3.24$) in figure 10(*a*,*b*) confirm this. The ratios (SL:U_{wt}/U_{op}) of the mean axial velocity magnitude integrated from the hub to the tunnel nozzle radius ($r/R = 3.00$) in table 6 confirm the increase in velocity magnitude with the VPWT being 7 % higher for the $J = -0.50$ case.

In the VPWT, nozzle blockage is identified as the second primary interference effect for an open propeller in crashback. In general, for an open-jet test section like the VPWT, this effect increases the magnitude of the free-stream velocity experienced by the model. It is also important to acknowledge that the effects of the collector can also be imperative in a similar way to the nozzle if the propeller and flow features like the vortex ring are located close enough, highlighting the importance of x_M from figure 2(*b*). Additional interference effects for symmetric solid models or bluff bodies in an open jet are detailed in Mercker *et al.* (1997), Wickern (2001) and Mokhtar & Britcher (2008).

4.6. Interference effects in crashback: impact on propeller loads

As discussed in the two previous sections, interference effects in crashback impact the magnitude of free-stream velocity U_∞ experienced by the propeller. The relationship between J and U_∞ in (1.1*a*,*b*)

https://doi.org/10.1017/flo.2024.36 Published online by Cambridge University Press

means that the propeller experiences a different advance ratio J, accordingly ($|J| \propto |U_\infty|$). In this section, we discuss the implications this has on the mean propeller loads and help shed light on the discrepancy observed between the VPWT experiments of Jessup *et al.* (2004, 2006) and the tow-tank experiments of Ebert *et al.* (2007).

Examining the mean load experimental data in figure 1(*a*), for $J < -0.50$, the trend observed is $|K_T| \propto |J|$ and $|K_Q| \propto |J|$. Solid blockage (jet expansion) causes a lower-magnitude U_∞. Since the propeller rotation rate n and propeller diameter D are the same for the VPWT and OW cases, this translates to a decrease in the magnitude of the advance ratio J. The mean loads (K_T and K_Q) for the VPWT case would then correspond to open-water or unconfined (OW) loads for a lower magnitude of J. The effect of nozzle blockage is opposite that of solid blockage, translating to mean loads for the VPWT case that correspond to OW loads for a higher magnitude of J. Overall, the load statistics from the VPWT experiments and the VPWT LES show a reduction in the magnitude of K_T and K_Q when compared with the OW cases. The magnitude of this reduction is most appreciable for the $J = -0.82$ case (table 4). For the $J = -0.50$ case, table 5 shows a consistent, though minor, reduction. This confirms that interference effects are more prominent for higher-magnitude J. Overall, this suggests that the effects of solid blockage or jet expansion (reduced $|J|$ and $|K_T|$ or $|K_Q|$) are dominant over those of nozzle blockage which counteracts it. These interference effects combine in a complex manner and some work in the literature has even suggested utilizing their relationship to reduce their overall impact by setting models in configurations where they cancel each other out (Wickern 2014).

4.7. Interference effects in crashback: the effective length scale of the vortex ring

Although the vortex ring has the effect of a solid model it is not easy to quantify its effects in the water tunnel. An effective length scale representative of the vortex ring region of influence is essential to properly assess the blockage ratio η and the severity of the interference effects. In this section, we explore an appropriate length scale.

The streamlines in figure 9(*a*,*b*) suggest that the vortex ring diameter is a good initial guess. Table 7 summarizes the vortex ring diameters (D_{vr}) and resulting blockage ratios (η_{vr}) determined from the circumferential averaged flow field of the four LES cases. The blockage ratio for the VPWT $J = -0.50$ case is then $\eta_{vr} = 0.20$ while for the VPWT $J = -0.82$ case it is $\eta_{vr} = 0.31$. In general, these are significant blockage ratios for models inside open-jet tunnels and would require corrections to the velocity or force measurements (Barlow *et al.* 1999; Mokhtar & Britcher 2008; Collin *et al.* 2016). The OW $J = -0.50$ and $J = -0.82$ cases have a much lower blockage ratio of $\eta_{vr} = 0.04$ and $\eta_{vr} = 0.03$, respectively.

The vortex ring traps a recirculating volume of fluid resulting in a similar volume displacement effect to a solid model. Therefore, it makes sense that an effective length scale can be estimated from this displaced volume. The circumferentially averaged flow statistics in figure 9(*a*,*b*) can be of use. Tracing the dividing streamline starting from the stagnation point upstream of the propeller to the downstream one, we can approximate the dimensions of the recirculating volume as an ellipsoid. The following are the approximate dimensions: for the VPWT $J = -0.50$ case, a volumetric diameter $D_{vol} \approx 2.25D$ and model length $L_M = 2.13D$ with $\eta_{vol} \approx 0.54$, while for the VPWT $J = -0.82$ case, a volumetric diameter $D_{vol} \approx 2.43D$ and $L_M = 2.10D$ with $\eta_{vol} \approx 0.64$ (table 7). These estimated blockage ratios are even larger than those using the vortex ring diameter and better represent the flow physical effect of the vortex ring in the VPWT.

For high-Reynolds-number, incompressible flows, the areas in the uniform free stream outside the thin surface boundary layers, and wakes of solid models are referred to as ideal. These areas meet the assumption that the flow is incompressible, inviscid and irrotational. Often, an effective model length scale represented by the extent of the surface of a model in the relevant direction represents well its region of influence on an oncoming free-stream flow, beyond which the flow can be considered ideal. For further inspection of the region of influence of the vortex ring, we can estimate the region of ideal flow

https://doi.org/10.1017/flo.2024.36 Published online by Cambridge University Press

Table 7. *All approximations were determined from the circumferentially averaged mean flow. The vortex ring diameter is D_{vr} and the blockage ratio η_{vr}. An approximate volume displacement diameter is D_{vol} and the blockage ratio η_{vol}. Using the OW cases, the vortex ring effective diameter $D_e \approx 3D_{vr}$ and blockage ratio η_e are approximated from the region of influence of the vortex ring from the circumferentially averaged mean flow calculation of the Bernoulli constant (figure 11c). It is also important to note that the area of the hub diameter at the location of the propeller is subtracted from all area calculations. The hub diameter is $D_h = 0.20D$, the tunnel nozzle diameter is $D_N = 3D$ and the OW case domain diameter is 7D.*

	Unconfined: $J = -0.50$	VPWT: $J = -0.50$	VPWT: $J = -0.82$	Unconfined: $J = -0.82$
D_{vr}	$1.52D$	$1.46D$	$1.75D$	$1.41D$
η_{vr}	0.04	0.20	0.31	0.03
D_{vol}	$\approx 2.32D$	$\approx 2.25D$	$\approx 2.43D$	$\approx 2.00D$
η_{vol}	≈ 0.10	≈ 0.54	≈ 0.64	≈ 0.07
D_e	$\approx 4.5D$	$\approx 4.3D$	$\approx 5.2D$	$\approx 4.25D$
η_e	≈ 0.4	≈ 2.2	≈ 3.0	≈ 0.4

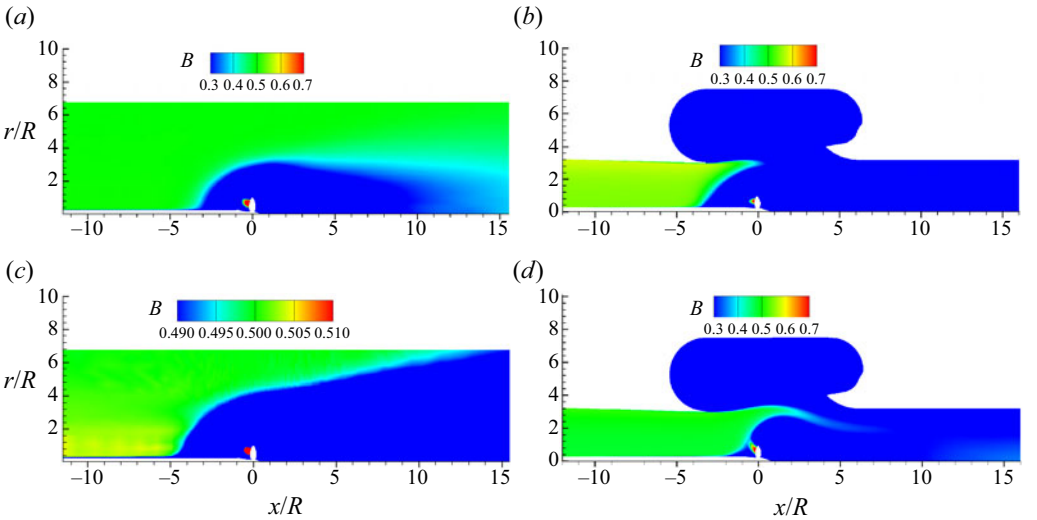

Figure 11. *The Bernoulli constant B calculated from the circumferentially averaged contours for (a) $J = -0.50$ OW case, (b) $J = -0.50$ VPWT case, (c) $J = -0.50$ OW case with a smaller contour range and (d) $J = -0.82$ VPWT case. The flow-field quantities are normalized appropriately using ρ and U_∞.*

around it by calculating the Bernoulli constant B using the circumferential average flow field (figure 11) as follows:

$$B = (p - p_\infty) + \tfrac{1}{2}\rho V^2, \tag{4.1}$$

where p is the pressure, ρ is the fluid density and V is the velocity magnitude, all quantities being normalized appropriately. This is the Bernoulli equation integrated along a streamline and assumes an ideal flow that is steady with no gravitational effects. In the far field, the assumptions of the Bernoulli equation remain valid, and $B = 0.5$ remains a constant (green in figure 11). Using a contour resolution of $B = \pm 0.01$ (figure 11c), the boundary of this region begins at $r/R \approx 4.5$ at the propeller plane ($x/R = 0.0$) and this distance grows radially larger while moving axially downstream along the wake of the OW case at $J = -0.5$ (figure 11c). We can call this approximate length scale the effective diameter

https://doi.org/10.1017/flo.2024.36 Published online by Cambridge University Press

of the vortex ring or D_e and its value is approximately three times the vortex ring diameter or $D_e \approx 3D_{vr}$ for both OW cases. This region likely varies according to the advance ratio with the trend of the vortex ring diameter size. Its high magnitude suggests that the unsteadiness of the vortex ring, as it breaks down and reforms, has a large region of influence that needs to be accounted for when estimating the blockage ratio. The larger boundary dimension of the OW case avoids affecting this region which explains why the results match well the OW experiments.

There are no regions of idealized flow in between the jet shear layer and vortex ring (figure 11*b*,*d*) for the VPWT cases. This is due to the effective length scale of the vortex ring ($D_e \approx 3D_{vr} \approx 4.4D - 5.3D$) which is much larger than the jet nozzle diameter ($D_N = 3D$) in the present cases. In addition, the jet shear layer thickness and its downstream growth further reduce the possible idealized flow region between the jet shear layer and the vortex ring. The consequence is that the interference effects in the VPWT experiments are those of a very high-blockage-ratio case, whether looking at the effective volume displaced or the region of influence of the vortex ring (table 7). This is why the effect on the loads is so large and why the present LES needed to include the VPWT geometry for validation. This also proves to be the case for the work of Kroll & Mahesh (2022), as the vortex ring diameter for a ducted propeller is larger than that for an open propeller due to the duct geometry. Overall, the vortex ring is dynamic and, as we have seen, its effects can span a large length scale.

5. Summary

Large-eddy simulation of a propeller was performed in crashback at $J = -0.50$ and $J = -0.82$, also utilizing an unstructured overset methodology. This is essential to capture the correct unsteady flow physics of crashback flow. To match experimental boundary conditions and study interference effects, the 36-inch VPWT geometry was included in the simulations. This is the first time to the authors' knowledge that this has been done in the literature. The LES force coefficient statistics are in good agreement with the experiments once the boundary conditions are matched for the VPWT and the open-water or unconfined (OW) conditions.

For the first time (to the authors' knowledge), the interference effects for a propeller in the crashback mode of operation have been identified and described, relating them to current knowledge and the literature on tunnel interference. First, the vortex ring and propeller-induced reverse flow impact are established to resemble that of a symmetric solid model or bluff body inside a tunnel. The interference effects are identified and established to be those that affect solid models. For the VPWT (an open-jet tunnel), two major interference effects are identified and verified, solid blockage through jet expansion and nozzle blockage. In general, the impact of interference effects on the tunnel flow field is to change the effective free-stream velocity U_∞ which also simultaneously changes the advance ratio J experienced by the propeller ($|J| \propto |U_\infty|$). This is confirmed for the solid blockage effect which decreases the magnitude of U_∞ (decreasing $|J|$) and nozzle blockage which increases the magnitude of U_∞ (increasing $|J|$). The corresponding impact on the loads ($|K_T| \propto |J|$) is confirmed and the discrepancy between the experiments of Jessup *et al.* (2004, 2006) and those of Ebert *et al.* (2007) is attributed primarily to the effects of solid blockage as the loads in the VPWT compare with a lower-magnitude J in unconfined or OW conditions. The strength of these interference effects is confirmed to vary with the advance ratio J and to be strongest for higher-magnitude J. These findings underline the complex flow physics in crashback and help explain the lack of theoretical, load data correction models like those in the design mode of operation.

There is a lack of crashback flow-field and load experimental data in the literature. Even with interference effects, the data in the VPWT (Jessup *et al.* 2004, 2006) provide enough of these details to help better understand crashback flow physics. However, this work has shown that the region of influence of the vortex ring is much larger than the propeller diameter D resulting in the VPWT cases resembling those of a very high-blockage-ratio setting. To help avoid and better assess the severity of the interference effects in future studies, it is suggested to estimate a more representative blockage ratio

https://doi.org/10.1017/flo.2024.36 Published online by Cambridge University Press

η. It is suggested that the length scale representative of the effects of the vortex ring is a value at least greater than the vortex ring diameter D_{vr} and more likely multiples of it.

It is important to note that several other lower-order interference effects can play a role in crashback, especially for an open-jet tunnel. Studying them in depth would require a parametric study with a significant computational cost due to the requirement of a modelling method like LES and the long crashback simulation times required for flow-field statistical convergence. This is why this work was restricted to only two advance ratios. Nevertheless, useful insight into the physical mechanisms behind interference effects in crashback has been revealed for the first time. This work also illustrates the importance of matching experimental boundary conditions to validate computational codes. In addition, this work helps highlight the role that LES and high-performance computing can play in future studies to help fill the gap of experimental work while also demonstrating the utility of LES as a potential, informative part of the design process of experiments and experimental facilities.

Acknowledgements. The authors would like to thank Dr W. Horne, Dr P. Kumar, Dr N. Morse and Mr M. Plasseraud for their thoughtful comments and discussions throughout this work.

Funding statement. This work was supported by the United States Office of Naval Research (ONR) under ONR grants N00014-18-1-2356 and N00014-21-1-2455 with Dr K.-H. Kim and Dr Y.L. Young as grant monitors. Computational resources were provided by the US Army Engineer Research and Development Center (ERDC) in Vicksburg, Mississippi on the Cray XC40/50, Onyx of High Performance Computing Modernization Program (HPCMP) and the Minnesota Supercomputing Institute (MSI) at the University of Minnesota.

Declaration of interests. The authors declare no conflict of interest.

Author contributions. T.B.K. created the grids, ran the simulations and post-processed the data. T.B.K. and K.M. wrote the manuscript.

Data availability statement. Raw data will not be available.

Ethical standards. The research meets all ethical guidelines, including adherence to the legal requirements of the study country.

References

Barlow, J., Rae, W.H. Jr. & Pope, A. 1999 *Low-Speed Wind Tunnel Testing*. John Wiley & Sons.

Chang, P., Ebert, M., Young, T.L., Liu, Z., Mahesh, K., Jang, H. & Shearer, M. 2008 Propeller forces and structural responses to crashback. In *Proceedings of the 27th Symposium on Naval Hydrodynamics, Seoul, Korea*.

Chen, B. & Stern, F. 1999 Computational fluid dynamics of four quadrant marine propeller flow. *J. Ship Res*. **43** (4), 218.

Collin, C., Mack, S., Indinger, T. & Mueller, J. 2016 Numerical and experimental evaluation of open jet wind tunnel interferences using the drivAer reference model. *SAE Intl J. Passeng. Cars-Mech. Syst*. **9**, 657–338.

Cooper, K. 1998 Bluff-body blockage corrections in closed- and open-test-section wind tunnels. AG-336, 6.1–6.34. AGARD.

Davoudzadeh, F., Taylor, L.K., Zierke, W.C., Dreyer, J.J., McDonald, H. & Whitfield, D.L. 1997 Coupled Navier–Stokes and equations of motion simulation of submarine maneuvers, including crashback. In *Proceedings of the 1997 ASME Fluids Engineering Division Summer Meeting*. ASME.

Donnelly, M., Jessup, S. & Etebari, A. 2010 Measurement of steady and unsteady duct loads for propeller 4381 at crashback conditions in the 36" water tunnel. *Tech. Rep.* NSWCCD-50-TR-2010/051. Naval Surface Warfare Center Carderock Division Hydromechanics Department Report.

Ebert, M., Chang, P. & Mulvihill, L. 2007 NSWCCD FY07 crashback computational effort. 2007 ONR Propulsor S&T Program Review, October.

Ewald, B. 1998 Wind tunnel wall corrections. AG-336. AGARD.

Fitzgerald, R.E. 2007 Wind tunnel blockage corrections for propellers. Masters thesis, University of Maryland.

Germano, M., Piomelli, U., Moin, P. & Cabot, W.H. 1991 A dynamic subgrid–scale eddy viscosity model. *Phys. Fluids* **A3** (7), 1760.

Glauert, H. 1933 Wind tunnel interference on wings, bodies, and airscrews. ARC R&M 1566.

Glauert, H. 1935 Airplane propellers. In *Aerodynamic Theory*. ARC R&M 1566.

Glauert, H. 1947 *The Elements of Aerofoil and Airscrew Theory*. Cambridge University Press.

Hecker, R. & Remmers, K. 1971 Four quadrant open-water performance of propellers 3710, 4024, 4086, 4381, 4382, 4383, 4384 and 4426. PNSRADC 417-H01. David Taylor Naval Ship Research and Development Center.

Horne, W.J. & Mahesh, K. 2019*a* A massively-parallel, unstructured overset method for Mesh connectivity. *J. Comput. Phys*. **376**, 585–596.

Horne, W.J. & Mahesh, K. 2019*b* A massively-parallel, unstructured overset method to simulate moving bodies in turbulent flows. *J. Comput. Phys.* **397**, 108790.

Jang, H. & Mahesh, K. 2012 Large eddy simulation of crashback in ducted propulsors with stator blades. In *Proceedings of the 29th Symposium on Naval Hydrodynamics, Gothenburg, Sweden*.

Jang, H. & Mahesh, K. 2013 Large eddy simulation of flow around a reverse rotating propeller. *J. Fluid Mech.* **729**, 151–179.

Jessup, S., Chesnakas, C., Fry, D. & Donnelly, M. 2006 Unsteady propeller performance in crashback conditions with and without duct. In *Proceedings of the 26th Symposium on Naval Hydrodynamics, Rome, Italy*.

Jessup, S., Chesnakas, C., Fry, D., Donnelly, M., Black, S. & Park, J. 2004 Propeller performance at extreme off design conditions. In *Proceedings of the 25th Symposium on Naval Hydrodynamics, St. John's, Canada*.

Jiang, C.W., Dong, R.R., Lui, H.L. & Chang, M.S. 1997 24-inch water tunnel flow field measurements during propeller crashback. In *Proceedings of the 21st Symposium on Naval Hydrodynamics*. The National Academies Press.

Kroll, T., Morse, N., Horne, W. & Mahesh, K. 2020 Large eddy simulation of marine flows over complex geometries using a massively parallel unstructured overset method. In *Proceedings of the 33rd Symposium on Naval Hydrodynamics, Osaka, Japan*.

Kroll, T.B. & Mahesh, K. 2022 Large-eddy simulation of a ducted propeller in crashback. *Flow* **2**, E-4.

Krynytzky, A. & Ewald, B. 1998 Conventional wall corrections for closed and open test sections. AG-336, 2.1–2.66. AGARD.

Kumar, P. & Mahesh, K. 2017 Large eddy simulation of propeller wake instabilities. *J. Fluid Mech.* **814**, 361–396.

Kumar, P. & Mahesh, K. 2018*a* Analysis of axisymmetric boundary layers. *J. Fluid Mech.* **849**, 927–941.

Kumar, P. & Mahesh, K. 2018*b* Large-eddy simulation of flow over an axisymmetric body of revolution. *J. Fluid Mech.* **853**, 537–563.

Lilly, D.K. 1992 A proposed modification of the Germano subgrid–scale closure model. *Phys. Fluids* **A4** (3), 633.

Lock, C.N.H. 1929 The interference of a wind tunnel on a symmetrical body. ARC/R&M-1275. H.M. Stationery Office.

Mahesh, K., Constantinescu, G. & Moin, P. 2004 A numerical method for large–eddy simulation in complex geometries. *J. Comput. Phys.* **197** (1), 215–240.

Mercker, E. 2013 On buoyancy and wake distortion in test sections of automotive wind tunnels. In *FKFS–9th Aerodynamic Conference*, pp. 205–227.

Mercker, E., Wickern, G. & Wiedemann, J. 1997 *Contemplation of Nozzle Blockage in Open Jet Wind-Tunnels in View of Different 'Q' Determination Techniques*. Society of Automotive Engineering.

Mokhtar, W.A. & Britcher, C.P. 2008 Boundary interference of high blockage models in open jet test sections. *SAE Intl J. Passeng. Cars-Mech. Syst.* **1**, 883–895.

Morse, N. & Mahesh, K. 2021 Large-eddy simulation and streamline coordinate analysis of flow over an axisymmetric hull. *J. Fluid Mech.* **926**, A18.

Morse, N. & Mahesh, K. 2023*a* Effect of tabs on the shear layer dynamics of a jet in cross-flow. *J. Fluid Mech.* **958**, A6.

Morse, N. & Mahesh, K. 2023*b* Tripping effects on model-scale studies of flow over the DARPA SUBOFF. *J. Fluid Mech.* **975**, A3.

Morse, N. & Mahesh, K. 2023*c* Large-eddy simulation of tripping effects on the flow over a 6:1 prolate spheroid at angle of attack. *J. Fluid Mech.* **960**, A3.

Park, N. & Mahesh, K. 2009 A proposed modification of the Germano subgrid–scale closure model. *Phys. Fluids* **21** (6), 065106.

Pergande, M., Wang, K., Neitzel-Petersen, J.C. & Abdel-Maksoud, M. 2017 Efficient prediction of crashback performance of controllable pitch propellers. In *Fifth International Symposium on Marine Propulsors, Espoo, Finland*.

Pontarelli, M., Martin, J.E. & Carrica, P.M. 2017 Dynamic instabilities in propeller crashback. In *Fifth International Symposium on Marine Propulsors, Espoo, Finland*, pp. 242–250.

Roshko, A. 1961 Experiments of flow over a circular cylinder at very high Reynolds numbers. *J. Fluid Mech.* **10**, 345–356.

Segalini, A. & Inghels, P. 2014 Confinement effects in wind-turbine and propeller measurements. *J. Fluid Mech.* **756**, 110–129.

Swithenbank, S.B., Jessup, S. & Etebari, A. 2008 Measurement of crashback loads on a blade of propeller 4381 in an open and ducted configuration in the 36-inch water tunnel. *Tech. Rep.* NSWCCD-50-TR2008/061. Naval Surface Warfare Center Carderock Division Hydromechanics Department Report.

Verma, A., Jang, H. & Mahesh, K. 2012 The effect of an upstream hull on a propeller in reverse rotation. *J. Fluid Mech.* **704**, 61–88.

Verma, A. & Mahesh, K. 2012 A Lagrangian subgrid-scale model with dynamic estimation of Lagrangian time scale for large eddy simulation of complex flows. *Phys. Fluids* **24** (8), 085101.

Vyşohlid, M. & Mahesh, K. 2006 Large eddy simulation of crashback in marine propellers. In *Proceedings of the 26th Symposium on Naval Hydrodynamics, Rome, Italy*.

Werle, M.J. 2011 Propeller wall-blockage performance corrections. *J. Propul. Power* **27**, 496–498.

Wickern, G. 2001 On the application of classical wind tunnel corrections for automotive bodies. SAE 2001-01-0633. Society of Automotive Engineering.

Wickern, G. 2014 Theoretical approach towards the self-correcting open jet wind tunnel. SAE 2014-01-0579. Society of Automotive Engineering.

Cite this article: Bahati Kroll T., Mahesh K (2025). A large-eddy simulation study of water tunnel interference effects for a marine propeller in crashback mode of operation. *Flow*, *5*, E2. doi:10.1017/flo.2024.36